



Temporal variation of aerosol properties at a rural continental site and study of aerosol evolution through growth law analysis

Jian Wang,¹ Don Collins,² David Covert,³ Robert Elleman,³ Richard A. Ferrare,⁴ Roberto Gasparini,² Hafliði Jonsson,⁵ John Ogren,⁶ Patrick Sheridan,⁶ and Si-Chee Tsay⁷

Received 23 September 2005; revised 31 March 2006; accepted 13 June 2006; published 23 September 2006.

[1] Aerosol size distributions were measured by a Scanning Mobility Particle Sizer (SMPS) on board the CIRPAS Twin Otter aircraft during 16 flights at the Southern Great Plains (SGP) site in northern central Oklahoma as part of the Aerosol Intensive Operation period in May 2003. During the same period a second SMPS was deployed at a surface station and provided continuous measurements. Combined with trace gas measurements at the SGP site and back trajectory analysis, the aerosol size distributions provided insights into the sources of aerosols observed at the SGP site. High particle concentrations, observed mostly during daytime, were well correlated with the sulfur dioxide (SO₂) mixing ratios, suggesting nucleation involving sulfuric acid is likely the main source of newly formed particles at the SGP. Aerosols within plumes originating from wildfires in Central America were measured at the surface site. Vertically compact aerosol layers, which can be traced back to forest fires in East Asia, were intercepted at altitudes over 3000 m. Analyses of size-dependent particle growth rates for four periods during which high cloud coverage was observed indicate growth dominated by volume controlled reactions. Sulfate accounts for 50% to 72% of the increase in aerosol volume concentration; the rest of the volume concentration increase was likely due to secondary organic species. The growth law analyses and meteorological conditions indicate that the sulfate was produced mainly through aqueous oxidation of SO₂ in clouds droplets and hydrated aerosol particles.

Citation: Wang, J., D. Collins, D. Covert, R. Elleman, R. A. Ferrare, R. Gasparini, H. Jonsson, J. Ogren, P. Sheridan, and S.-C. Tsay (2006), Temporal variation of aerosol properties at a rural continental site and study of aerosol evolution through growth law analysis, *J. Geophys. Res.*, *111*, D18203, doi:10.1029/2005JD006704.

1. Introduction

[2] Atmospheric aerosols affect the global energy budget by scattering and absorbing sunlight (direct effect) and by changing the microphysical structure, lifetime, and coverage of clouds (indirect effect). While it is widely accepted that aerosols could have significant impact on global climate, at present the magnitudes of these effects are poorly understood. Unlike greenhouse gases, whose radiative forcing can be calculated with high accuracy, there are substantial uncertainties associated with predicted aerosol radiative forcing, especially the indirect forcing resulting from the

interaction of aerosols and clouds. The Intergovernmental Panel on Climate Change (IPCC) estimated that the direct and indirect effects of aerosols remain the most uncertain components in forcing of climate change over the industrial period [*Intergovernmental Panel on Climate Change*, 2001]. The large uncertainties in aerosol direct and indirect effects are combinations of the present fragmented understanding of the interactions among aerosol, radiation, and clouds, and the large uncertainties in knowledge of aerosol properties and global distributions. Compared to greenhouse gases such as CO₂, the lifetime of atmospheric aerosol is very short, about a week. As a result, the temporal and spatial distributions of atmospheric aerosol and its properties are inhomogeneous and highly variable. Predictions of future aerosol effects require detailed understanding of aerosol properties and geographical distributions, as well as of the processes that control the evolution of aerosols. Among aerosol properties, aerosol size distribution is one of the most important parameters needed for assessing aerosol climate effects. Aerosol size distribution influences climate forcing through its effects on light scattering and modification of cloud microphysical properties affecting albedo and persistence.

[3] The Southern Great Plains (SGP) Climate Research Facility is the first and largest of such facilities established

¹Atmospheric Science Division, Brookhaven National Laboratory, Upton, New York, USA.

²Department of Atmospheric Sciences, Texas A&M University, College Station, Texas, USA.

³Department of Atmospheric Sciences, University of Washington, Seattle, Washington, USA.

⁴NASA Langley Research Center, Hampton, Virginia, USA.

⁵Naval Postgraduate School, Monterey, California, USA.

⁶Global Monitoring Division, Earth System Research Laboratory, NOAA, Boulder, Colorado, USA.

⁷NASA Goddard Space Flight Center, Greenbelt, Maryland, USA.

by the Atmospheric Radiation Measurement (ARM) Program. The SGP Climate Research Facility covers an area of $\sim 142,000 \text{ km}^2$ in North Central Oklahoma and South Central Kansas. The central facility at SGP is located at 36.60°N and 97.48°W , with an altitude of 319 m. Since 1992, continuous measurements have been carried out, which provide a long time record of aerosol, cloud, radiation, and atmospheric properties at the SGP. These measurements have been used in many aerosol studies including quantification of the aerosol indirect effect [Feingold *et al.*, 2003; Kim *et al.*, 2003], studies of vertical aerosol extinction and backscattering [Turner *et al.*, 2001, 2002], and the application of surface measurements to retrieve aerosol optical depth [Bergin *et al.*, 2000]. From 5 to 31 May 2003, an Aerosol Intensive Operation Period (IOP) was conducted at the SGP [Ferrare *et al.*, 2006a]. During the IOP, additional instruments were deployed both at surface sites and on board a research aircraft. The additional measurements included submicrometer aerosol size distribution, hygroscopicity, chemical composition, and optical properties. In addition to aerosol measurements, the mixing ratios of relevant trace gases were also monitored at a NASA mobility facility during the IOP. The simultaneous measurements of the wide range of aerosol properties not only provided detailed characterizations of aerosols during spring time, but also allowed studies of aerosol evolution processes at the SGP.

[4] In this paper, we present both continuous records at surface and vertical profiles of aerosol size distribution measured during the IOP at the SGP site. On the basis of back trajectory analyses, the air masses that arrived at the SGP site were grouped into 4 classes. For each class, the source and the evolution process of the aerosol are discussed using simultaneous aerosol and trace gas measurements. During the IOP, plumes from distant fire activities were detected both at the surface and in elevated layers at altitudes over 3000 m. Aerosols within these plumes showed high scattering coefficients and large accumulation-mode diameters and concentrations. The characteristics of the aerosols observed within these plumes are presented. We also carried out detailed particle growth law analyses for four cases using the continuous measurements of aerosol size distribution at the surface. The results of the growth law analyses provide insights into the aerosol evolution processes at the SGP.

2. Measurements

2.1. Aerosol Size Distribution Measurements

[5] Among the instruments deployed during the IOP were two Scanning Mobility Particle Sizers (SMPS). One of the two SMPS was operated on board a Twin Otter aircraft to characterize the vertical profiles and horizontal variability of aerosol size distribution in the vicinity of the SGP site. The Twin Otter aircraft is operated by the Center for Interdisciplinary Remotely Piloted Aircraft Studies (CIRPAS) based at Marina, California [Bluth *et al.*, 1996], and performed 16 research flights out of Ponca City airport, Oklahoma (32 km east of the SGP central facility). Most of the flight patterns were centered on the central facility at the SGP site. The details of the Scanning Mobility Particle Sizer on board the Twin Otter is given by Wang *et al.* [2003]. The major

components of the airborne SMPS system are a cylindrical Differential Mobility Analyzer (TSI Inc., model 3081) and a condensation particle counter (TSI Inc., model 3010). Prior to measurements, the relative humidity (RH) of the aerosol sample was reduced to below 25% inside a Nafion drier. The second SMPS was deployed at the surface GIF, which is located at the SGP site central facility (36.60°N , 97.48°W , 319 m). The SMPS at GIF provided continuous measurements of submicrometer aerosol size distributions from 6 to 27 May, except for a few brief periods of instrument downtime. The only significant difference between the two SMPS systems is that no Nafion drier was installed in the SMPS at the GIF. The relative humidity (RH) inside the SMPS at the GIF was lower than the ambient RH as a result of the higher temperature inside the instrument. The SMPS on board the Twin Otter measured aerosol size distribution ranging from 20 nm to 800 nm every 73 s; the SMPS at the GIF had a time resolution of 2 min for particles ranging from 25 nm to $1 \mu\text{m}$. Both SMPS systems were carefully calibrated during the IOP using Polystyrene Latex standards. Data from both SMPS systems were analyzed using the data inversion procedure described by Collins *et al.* [2002]. A comparison between the size distributions measured by the two SMPS systems during the IOP is shown in Figure 1. The aerosol size distributions were averaged from 0957 to 1012 LT on 20 May 2003 (local daylight saving time, GMT-5hrs will be used throughout this paper). During the period, the Twin Otter flew an overpass above the GIF at an altitude of 200 m above ground level (AGL). Two vertical profiles of potential temperature were measured on board Balloon-Borne Sounding Systems (BBSS) at 0630 and 1230 LT, respectively. The potential temperature profiles suggest vertical homogeneity from the surface to the altitude of 200 m (AGL). The relative humidity (RH) inside both instruments was below 25%. The aerosol size distributions were bimodal, and good agreement was found between the measurements from the two SMPS.

2.2. Related Aerosol Measurements

[6] Besides the aerosol size distributions, aerosol optical properties measured at the GIF and on board the Twin Otter are also used in this study. As part of the long-term aerosol measurements at the SGP site (since 1996), aerosol scattering, absorption, and scattering $f(\text{RH})$ have been measured continuously at the Aerosol Observation System (AOS) trailer, which is located approximately 150 m from the GIF at the SGP site [Sheridan *et al.*, 2001]. The $f(\text{RH})$ is defined as:

$$f(\text{RH}) = \sigma_{sp(\text{RH}=85\%)} / \sigma_{sp(\text{RH}=40\%)} \quad (1)$$

where $\sigma_{sp(\text{RH}=85\%)}$ and $\sigma_{sp(\text{RH}=40\%)}$ are aerosol scattering coefficients at RH of 85% and 40%, respectively. During the IOP, an additional nephelometer and Particle/Soot Absorption Photometer (PSAP) at low RH conditions were set up in the GIF. The details of the aerosol optical property measurements at the AOS and the GIF during the IOP are given by Andrews *et al.* [2006]. On board the Twin Otter aircraft, aerosol scattering, absorption, and scattering $f(\text{RH})$ were measured by a 3-wavelength nephelometer, a PSAP, and a humidigraph, respectively. The description of the

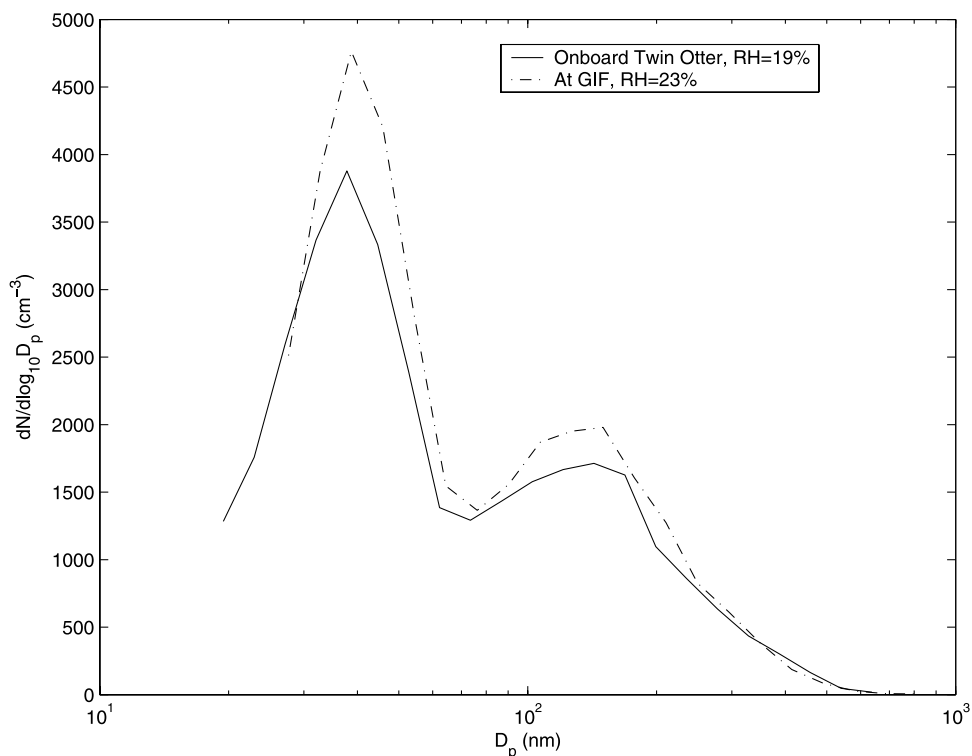


Figure 1. Comparison of the aerosol size distributions measured by the SMPS on board the Twin Otter (solid line) to that measured at the GIF (dashed line). The aerosol size distributions were averaged from 0957 to 1012 LT on 20 May 2003. During this period, the Twin Otter flew over the GIF at an altitude of 200 m above ground level (AGL).

airborne aerosol optical property measurements is given by Schmid *et al.* [2005]. The size cut for the nephelometer and PSAP measurements at the AOS trailer and the GIF were alternated between 1 μm and 10 μm every 6 min. All in situ instruments on board the Twin Otter sampled from a common inlet. The particle transmission efficiency of the inlet is nearly 100% for particles smaller than 3.5 μm , and 60% for particle of 5.5 μm in diameter for typical Twin Otter velocity of 50 m/s [Hegg *et al.*, 2005].

2.3. Related Trace Gas Measurements

[7] Mixing ratios of trace gases, including CO and SO₂ used in this study, were monitored at a NASA mobility facility located approximately 50 m from the GIF. The CO mixing ratio was measured by a CO analyzer (Thermo Environmental Inc, model 48C) that was calibrated with a NIST-ratioed CO standard. Data were logged every 5 min. The mixing ratio of SO₂ was monitored using a SO₂ analyzer (Thermo Environmental Inc, model 43C) that was calibrated with a NIST-ratioed SO₂ standard. No chemical zero was installed prior to 18 May 2003. After that date, a K₂CO₃-impregnated filter that removes all SO₂ from the gas stream was installed and the SO₂ analyzer was zeroed periodically by switching the inlet flow to pass through the filter. As a result, the SO₂ mixing ratios measured after 18 May are considered more accurate than those measured before 18 May. The uncertainties associated with the SO₂ measurements before and after 18 May are estimated to be 0.5 ppb and 0.05 ppb, respectively. Because of the large uncertainties in the SO₂ measurements relative to the observed mixing

ratios, the SO₂ mixing ratios measured during the IOP are only used qualitatively in this study.

3. Results and Discussion

3.1. Size Distribution Measured at Surface

[8] Aerosol number size distributions, aerosol scattering coefficients ($D_p < 10 \mu\text{m}$) at three wavelengths, and total particle number concentrations measured at the GIF during the IOP are shown in Figure 2. The aerosol size distributions were adjusted to dry conditions using the measured hygroscopicity [Gasparini *et al.*, 2006]. The aerosol scattering coefficients were measured at RH mostly below 50% during the IOP. The precipitation, which is routinely measured at the SGP site, is also presented. During the IOP, substantial variations were observed in aerosol properties, including aerosol size, concentration, and scattering coefficients. The aerosol scattering coefficient at 550 nm ranged from 2.1 to 413 Mm^{-1} , with the highest level of 413 Mm^{-1} observed on 8 May. This level substantially exceeds the 95 percentile (less than 150 Mm^{-1} at 550 nm) of a 4-year record at the SGP site [Sheridan *et al.*, 2001]. During the same period on 8 May, the dry aerosol size distribution exhibited an accumulation-mode diameter of 200 nm, which was the largest observed at the surface during the IOP. The sources of the aerosol during this period are discussed later. There were two major precipitation events during the IOP, 16 and 24 May. Following these precipitation events, substantial decreases in aerosol scattering coefficients were observed; following the precipitation on 16 and 24 May, the

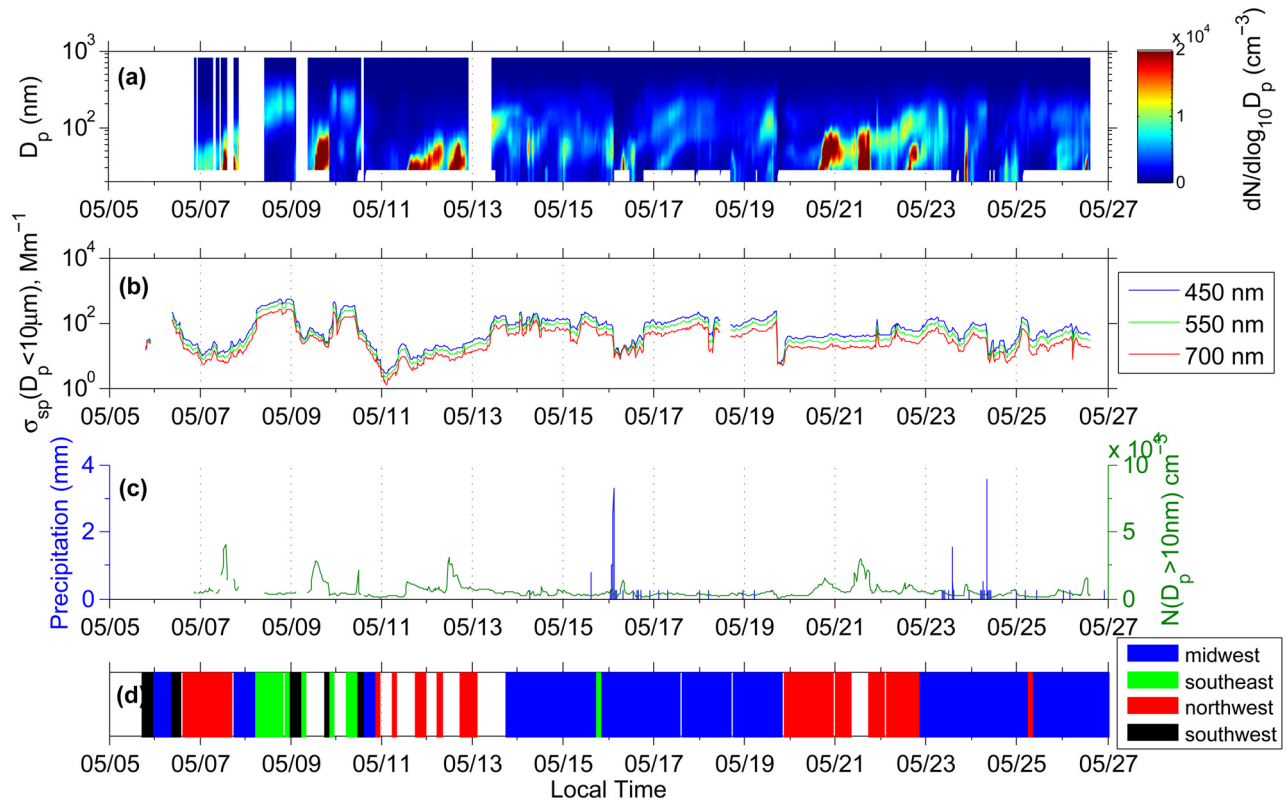


Figure 2. Measurements from 6 to 27 May 2003 at the SGP surface sites. (a) Aerosol number size distributions measured by SMPS, adjusted to dry conditions. (b) Aerosol scattering coefficients ($D_p < 10 \mu\text{m}$) measured by a 3-wavelength nephelometer at RH mostly below 50%. (c) Precipitation and total particle number concentration measured by a condensation particle counter. (d) Classification of air mass based on back trajectory analyses. Note in Figure 2a, the maximum concentration in the color scale is set at $20,000 \text{ cm}^{-3}$ in order to show details of the size distribution evolution.

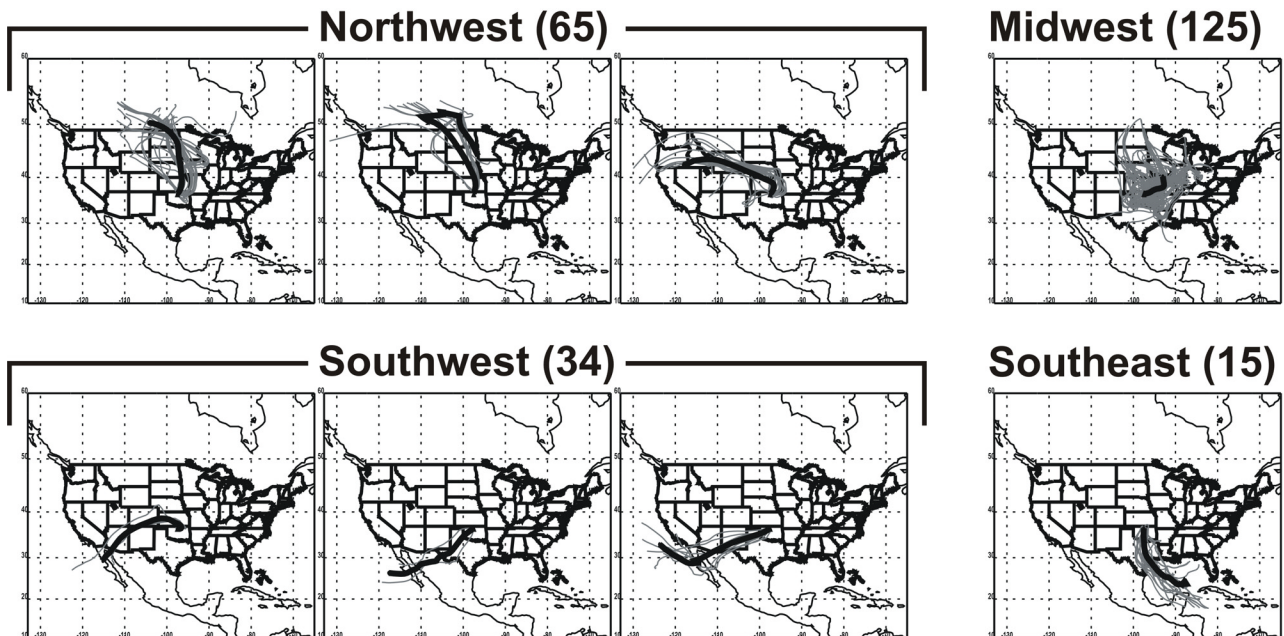


Figure 3. Eight clusters of 219 back trajectories and their grouping into four back trajectory classes. The back trajectories were calculated for air parcels arriving at the SGP site 150 m AGL every 3 hours during the IOP.

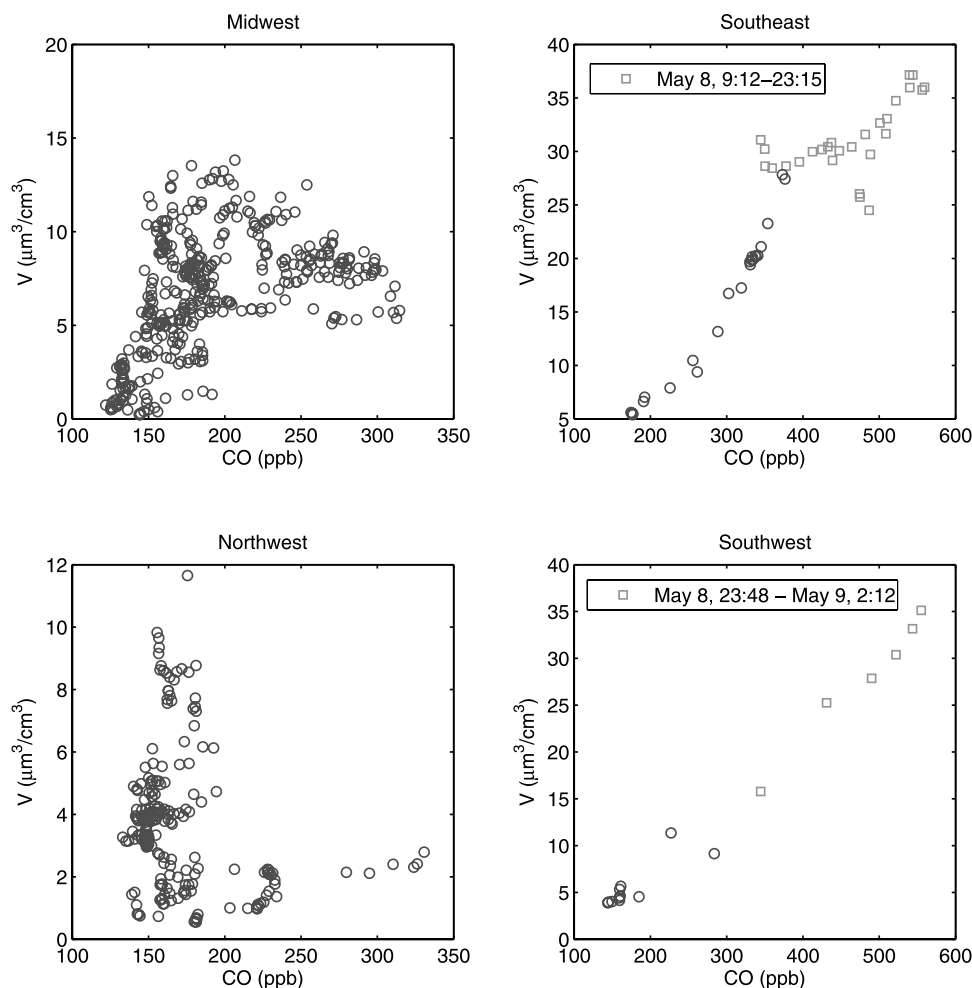


Figure 4. Submicrometer aerosol volume concentration plotted against simultaneous measurements of CO mixing ratio for each air mass class.

aerosol scattering coefficient at 550 nm decreased from 67 to 9.7 Mm^{-1} and from 62 to 8.1 Mm^{-1} , respectively. These decreases are attributed to wet deposition. High particle number concentrations were frequently observed during the IOP, often coincident with the observations of nucleation mode particles.

[9] On the basis of back trajectory analysis, air masses arriving at the SGP site during the IOP were grouped into four classes (Figure 2) [Gasparini *et al.*, 2006]. The back trajectories of parcels arriving at the SGP Central Facility 150 m above ground level (AGL) were calculated using the NOAA HYSPLIT4 model [Draxler, 1988] at 3-hour intervals for the entire IOP. In order to establish the dominant profiles among these 219 back trajectories, similar back trajectories were grouped using the cluster analysis technique described by Dorling *et al.* [1992]. This analysis resulted in eight distinct back trajectory clusters. Because of the small number of observations associated with several of the back trajectory clusters, some of the visually similar clusters were merged into four classifications that were more statistically significant. These classes represent back trajectories from the Northwest, Midwest, Southeast, and Southwest. Maps showing the original eight clusters and their grouping into the four back trajectory classifications are presented in Figure 3.

[10] The dry submicrometer aerosol volume concentration is plotted against the simultaneously measured CO mixing ratios for each air mass class (Figure 4). The aerosol volume concentrations are calculated from aerosol number size distributions measured by the SMPS at the GIF. The aerosol size distributions were adjusted to dry conditions using the hygroscopicity measured by a Tandem Differential Mobility Analyzer [Gasparini *et al.*, 2006], and were averaged into 30-min time intervals. For air masses from the Southeast, the submicrometer aerosol volume concentration was well correlated with the measured CO mixing ratio, which suggests the aerosols were mainly produced through combustion processes. During 0912 to 2315 LT on 8 May, high submicrometer aerosol volume concentration up to $37.2 \mu\text{m}^3/\text{cm}^3$ was observed concurrent with the air mass being from the southeast. During the same period, the CO mixing ratio reached 560 ppb, and the aerosol scattering coefficient and the accumulation mode diameter also reached the highest levels observed at the GIF during the IOP. Back trajectory analysis indicates the air mass arriving at the SGP during this period originated in Central America on 6 May, at which time extensive wildfires were reported in Central America. The extensive wildfires are clearly shown in a picture taken by Moderate Resolution Imaging Spectroradiometer (MODIS) on 5 May 2003 (<http://rapidfire>.

Table 1. Statistics of Fitted Aerosol Number Size Distributions During the IOP

Mode and Parameters	Midwest	Southeast	Southwest	Northwest
Nucleation Occurrence	47%	69%	35%	52%
Aitken Occurrence	83%	76%	71%	92%
$D_{p,i}$, nm	69 ± 29	90 ± 53	51 ± 11	62 ± 30
N_i , cm ⁻³	2304 ± 1620	1368 ± 693	6952 ± 6022	3369 ± 3358
σ_i	1.73 ± 0.36	1.84 ± 0.47	1.65 ± 0.36	1.46 ± 0.27
Accumulation Occurrence	93%	100%	71%	91%
$D_{p,i}$, nm	165 ± 40	209 ± 33	199 ± 13	151 ± 38
N_i , cm ⁻³	1202 ± 913	2301 ± 1368	1841 ± 1263	749 ± 794
σ_i	1.52 ± 0.17	1.47 ± 0.13	1.51 ± 0.04	1.53 ± 0.12
Number of size distributions	481	51	17	205

sci.gsfc.nasa.gov/gallery). Using a coupled aerosol, radiation, and meteorology model, Wang *et al.* [2006] simulated the transport of the Central American smoke during 20 April to 21 May 2003. They found the modeled Aerosol Optical Thickness (AOT) consistently captured the fluctuations of the measured AOT, and the model-simulated timeline of the smoke events (e.g., 8–12 May 2003) is in good agreement with those identified from observed AOTs at the SGP site. The simultaneous observations of high submicrometer aerosol volume concentration and CO mixing ratio, combined with the back trajectory analysis and the modeling results, give strong support to the attribution of the observation to smoke transported from Central America. Aerosol compositional analyses by synchrotron x-ray fluorescence of aerosol samples collected at the surface by a rotating DRUM sampler [Cahill *et al.*, 1985; Raabe *et al.*, 1988; Cahill and Wakabayashi, 1993; Bench *et al.*, 2001] showed that this period had high nonsoil potassium indicative of a strong biomass burning signature (T. A. Cahill *et al.*, unpublished report, 2004).

[11] When the air mass was from the southwest, the submicrometer aerosol volume concentration was also highly correlated with CO mixing ratio. From 8 May at 2348 LT to 9 May at 0212 LT, high CO mixing ratio and submicrometer aerosol volume concentration were again observed. The CO mixing ratio ranged from 345 ppb to 555 ppb, and the submicrometer aerosol volume concentration was 15.8 to 35.1 $\mu\text{m}^3/\text{cm}^3$. Except during the two periods described above, the CO mixing ratio measured during the IOP was mostly below 350 ppb.

[12] For air masses from the northwest, the CO mixing ratio was mostly between 133 and 200 ppb, and the submicrometer aerosol volume concentration varied from 0.55 to 11.7 $\mu\text{m}^3/\text{cm}^3$. The low CO mixing ratio measured is expected as there are no major CO sources (such as vehicle emissions from urban areas) toward the northwest, and no fire events were reported in the region during the IOP. The large variation in aerosol volume concentration and the relatively constant and low CO mixing ratio suggest that the aerosol was produced mainly through processes other than combustion. For a small fraction of the measurements, the CO mixing ratio reached 300 ppb. Although it is not possible to pinpoint the exact reason, the occasional observations of such high CO mixing ratio could be due to

mixing of the air parcel with vehicle emission from local traffic. The Midwest class consisted of more than 50% of the measurements during the IOP. The poor correlation between the submicrometer aerosol volume concentration and the CO mixing ratio is likely due to the following reasons. In Midwest region, CO is mainly produced through combustion processes and from cities, which are not significant sources of aerosol volume when compared to power plants. Most Midwest power plants emit substantial SO₂ but have low CO emission rates.

3.2. Statistics of Aerosol Number Size Distribution During the IOP

[13] Aerosol size distributions measured at the GIF were fitted with up to three log normal functions to derive statistics:

$$\frac{dN}{d \log_{10} D_p} = \sum_{i=1}^3 \frac{N_i}{\sqrt{2\pi} \log_{10} \sigma_i} \exp \left[-\frac{(\log_{10} D_p - \log_{10} D_{p,i})^2}{2 \log_{10}^2 \sigma_i} \right] \quad (2)$$

where N_i , $D_{p,i}$ and σ_i are the mode number concentration, geometric mean diameter, and geometric standard deviation, respectively. Prior to the fitting, the measured aerosol size distributions were adjusted to dry conditions using the measured hygroscopicity [Gasparini *et al.*, 2006]. The adjusted aerosol size distributions were then averaged into 30-min intervals. During the IOP, the size distributions observed are described with three modes: a nucleation mode ($D_p = 5\text{--}30$ nm), an Aitken mode ($D_p = 30\text{--}100$ nm), and an accumulation mode ($D_p = 100\text{--}500$ nm). The statistics of the fitted modes are presented in Table 1 for each air mass class. As the nucleation modes often exhibited a mode diameter below 20 nm and were not completely captured by the SMPS, only the frequency of the appearance of a nucleation mode is considered accurate and is given in Table 1. The nucleation mode was frequently observed during the IOP for each air mass class. The mode diameter and the concentration of both Aitken and accumulation modes showed substantial variations. The average accumulation mode diameters for the Southeast and Southwest classes are 209 and 199 nm, respectively, which are substantially larger than those when air masses originated from the Midwest and Northwest. The larger accumulation mode diameters of the Southeast and Southwest classes were due to the influence of the extensive fire activities in Central America described above. Despite the large differences in the accumulation mode diameter and concentration, the geometric standard deviation of the accumulation mode showed little variation among the four classes. The average geometric standard deviation of geometric standard deviation is about 1.50 for all four classes, a value close to the “self-preserving size distribution” geometric standard deviation of 1.34 [Hinds, 1999].

3.3. High Particle Number Concentration Events Observed During IOP

[14] During the IOP, high particle number concentrations, over 15,000 cm⁻³, were observed 7 times. Figure 5 shows an example of the observed high particle number concentrations, which reached 40,000 cm⁻³ at 1300 LT on 7 May.

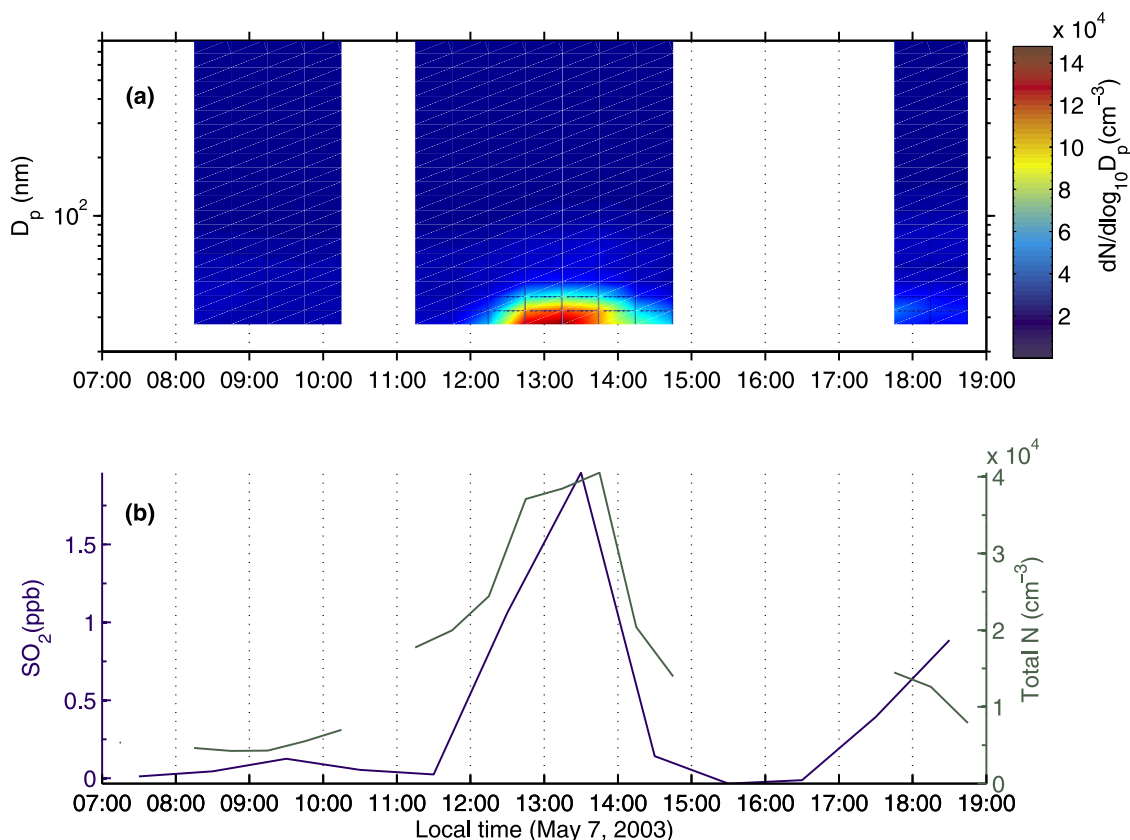


Figure 5. Measurements during a nucleation event from 0700 to 1900 LT on 7 May. (a) Dry aerosol number size distributions with the color indicating the number concentration. (b) SO_2 mixing ratio and number concentration of particles having diameters greater than 10 nm.

At the same time, a peak in SO_2 mixing ratio was recorded, and aerosol number size distribution showed a peak diameter near or below the 20 nm of the lower size range of the SMPS. The high concentration of small particles suggests new particle formation through homogeneous nucleation. For each of the 7 cases, a peak in SO_2 mixing ratio was observed along with high particle number concentrations and small peak diameters. Six of the seven cases were observed from 1130 to 1530 LT, with the remaining one observed around 1745 LT. In contrast, there were two periods during which the SO_2 mixing ratios peaked at over 1 ppb while the total particle number concentrations remained below 8000 cm^{-3} . One of the two periods was at about midnight and the other period was around 2000 LT. As the high particle concentrations were observed mostly during day time and were coincident with enhanced SO_2 mixing ratios, we think new particles were generated through homogenous nucleation involving sulfuric acid. The sulfuric acid vapor is produced through oxidation of SO_2 by OH radical, which is produced in sunlight. The newly formed particles then grew into the measurement range of the SMPS through coagulation and condensation. The possible nucleation mechanisms include binary $\text{H}_2\text{SO}_4\text{-H}_2\text{O}$ and ternary nucleation of H_2SO_4 , NH_3 , and H_2O , as suggested by previous field studies [Clarke *et al.*, 1999; Weber *et al.*, 1999, 2001; Kulmala *et al.*, 2002].

[15] Figure 6 shows the maximum SO_2 mixing ratio and total particle number concentrations measured during the

IOP as a function of the wind direction. High SO_2 mixing ratio and particle number concentrations were observed when the wind was from the east, south, and southwest. The similar distributions of the SO_2 and particle number concentrations as functions of wind direction support our conclusion that the high particle concentrations were results of particle formation through homogeneous nucleation involving sulfuric acid. Several power plants are located to the east, south, and southwest of the SGP site. To the east of the SGP site are three power plants named Conoco, Ponca, and Sooner. The Sooner power plant has the highest SO_2 emission rate of 24 kiloTons/year (kT/year, 1999 EPA emission inventory). All three power plants are within 45 km of the SGP site. To the Southwest near Enid, Oklahoma is the Kremlin plant with an emission rate of 6.5kT/yr, and to the south of the SGP site is the Mustang plant in Oklahoma City, which has a SO_2 emission rate of 5.0 kT/yr. The observed excursions of SO_2 mixing ratio are thus due to the emissions from these or other power plants in the vicinity of the SGP site. When the wind is from east to east-southeast, the emission from Sooner is likely to dominate the SO_2 concentration.

3.4. Vertical Profiles of Size Distribution Measured On Board the Twin Otter

[16] In addition to continuous measurements at the surface, a SMPS was deployed on board the Twin Otter aircraft to characterize the vertical profiles of aerosol size distribu-

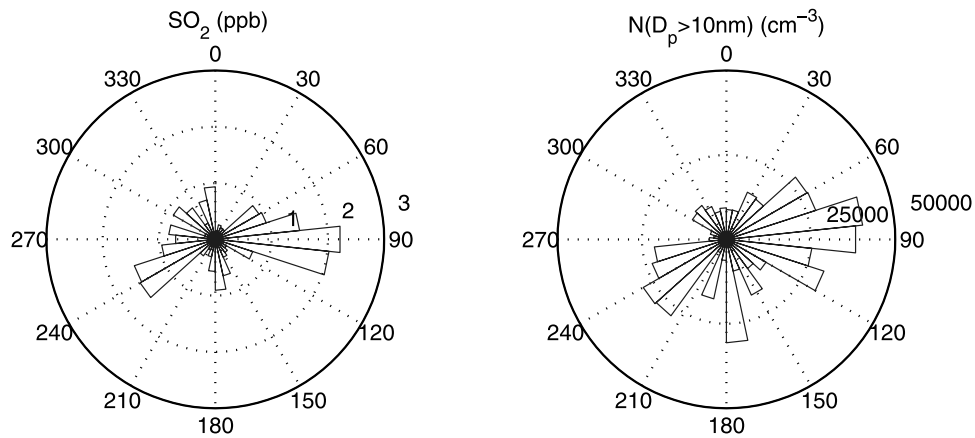


Figure 6. Maximum SO_2 mixing ratio and particle number concentrations measured during the IOP as functions of wind direction.

tion. During the IOP, 16 research flights were flown out of the Ponca City airport, Oklahoma. Most of the research flights started between 0900 to 1100 LT in the morning and ended in the early afternoon. As is typical for a continental

site in late spring, the boundary layer was often stable in the morning, as evidenced by an increasing potential temperature with increasing altitude. As the surface heating increased, the boundary layer gradually became well mixed

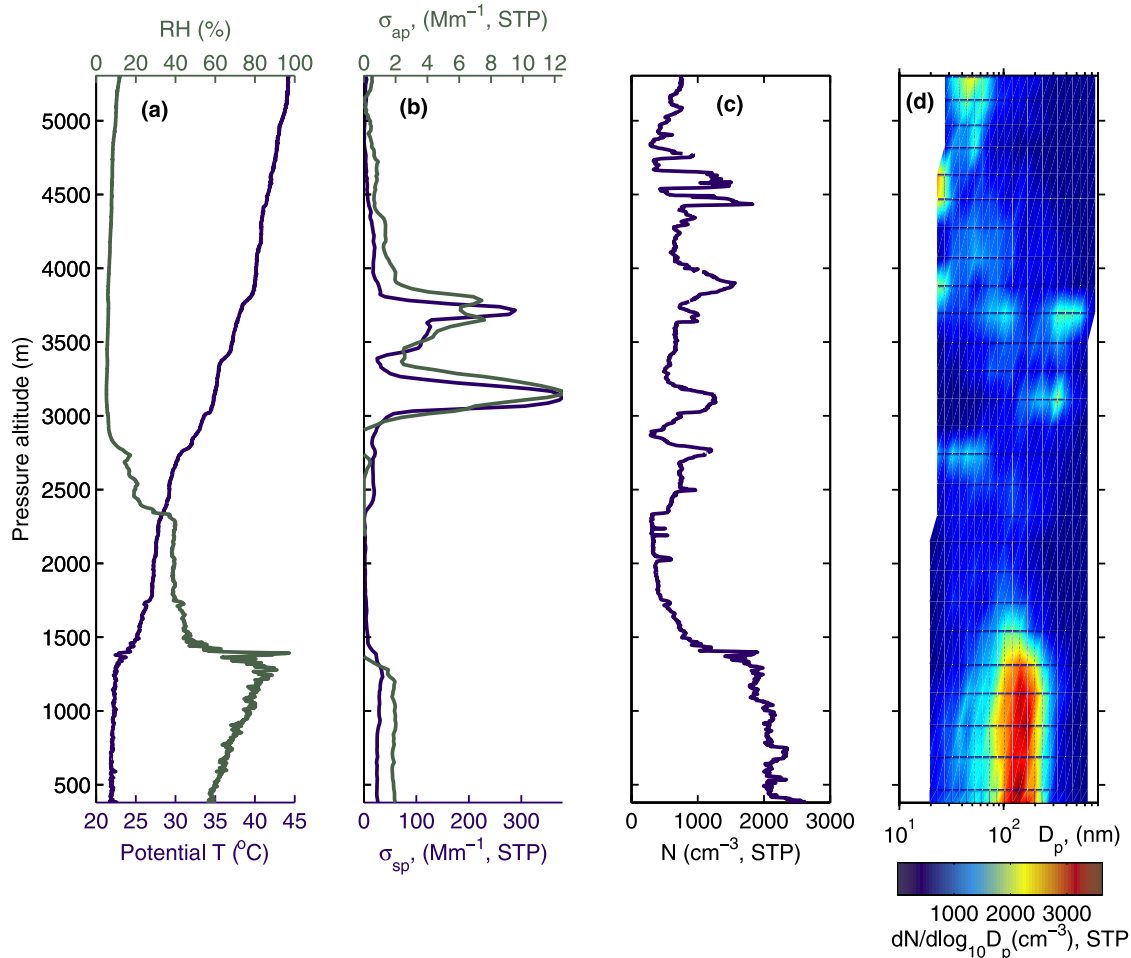


Figure 7. Vertical profiles of measurements taken during an ascent from 1540 to 1612 LT on 25 May 2003. (a) Relative humidity and potential temperature; (b) aerosol scattering and absorption coefficients at 530 nm, adjusted to STP (0°C and 1 atm); (c) number concentration of particles having diameters greater than 10 nm, measured by a Condensation Particle Counter, concentration adjusted to STP; and (d) aerosol number size distribution adjusted to STP.

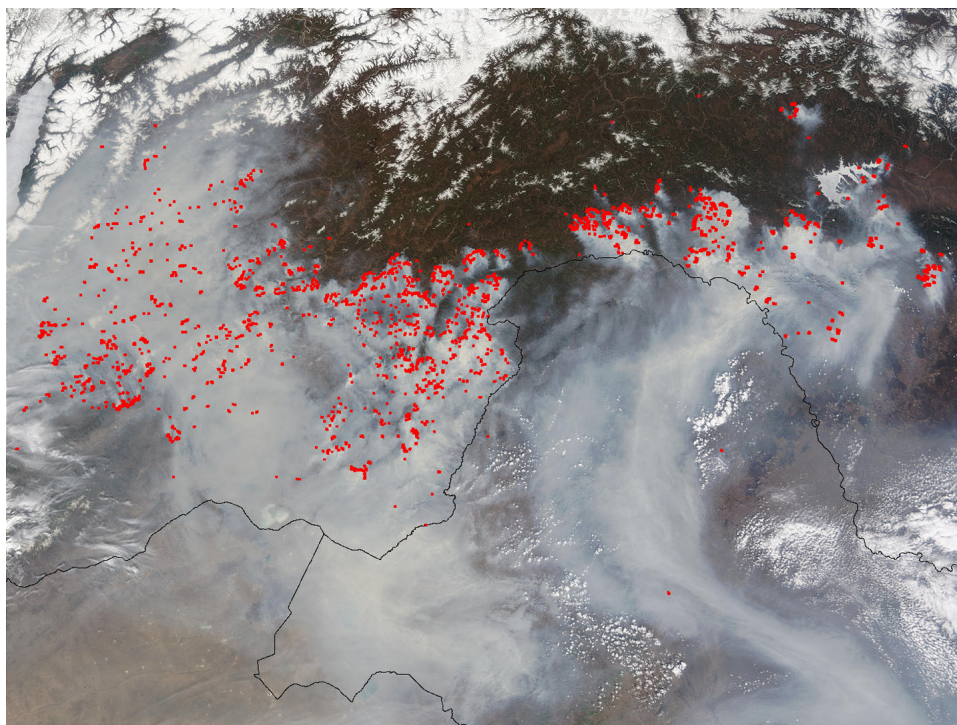


Figure 9. Extensive forest fires in Russia near the border with China shown in a picture taken by Moderate Resolution Imaging Spectroradiometer (MODIS) on board Terra Satellite on 14 May 2003 (from online MODIS rapid response system gallery, NASA).

(adjusted to STP), which is more than 6 times that in the boundary layer. In contrast, the total particle number concentrations within each of the two layers were much lower than those in the boundary layer, about 2000 cm^{-3} (also adjusted to STP). The aerosol size distributions showed a fairly rich structure in the free troposphere. In the two layers with elevated light scattering coefficients, the accumulation mode diameters were nearly 400 nm, which accounts for the observed high aerosol scattering coefficients despite the low number concentrations.

[18] To understand the origin of the elevated aerosol layers, we carried out back trajectory calculations using NOAA HYSPLIT4 model. The back trajectory calculation (Figure 8) indicates the aerosol layers observed originated 11 days earlier from Northeast Asia near the border of China and Russia [Damoah *et al.*, 2004; Jaffe *et al.*, 2004]. Figure 9 is a picture taken by Moderate Resolution Imaging Spectroradiometer (MODIS) on board the Terra Satellite on 14 May, which indicates extensive forest fires in Russia near the Chinese border. The calculated trajectories over Northeast Asia are at an altitude of 9 km, which is substantially higher than typical particle injection heights. Despite the discrepancy in the trajectory height and substantial uncertainties associated with back trajectory calculations over such an extended period, the high aerosol scattering coefficient and large accumulation-mode diameter at high altitude suggest a forest fire as the only plausible source. The large accumulation-mode diameter, which is up to 400 nm, is likely a result of particle coagulation and condensation of gas phase species during the transport from northeast Asia to above the SGP site, and is consistent with other obser-

vations of long-range transport of aged smoke [Wandinger *et al.*, 2002; Murayama *et al.*, 2004; Mattis *et al.*, 2003].

[19] Elevated aerosol layers with high scattering and absorption coefficients were also observed during two other flights on 27 and 28 May 2003. On the basis of similar considerations, these elevated layers are also attributed to plumes from the forest fires in the same area in East Asia. The aerosol optical properties averaged over the elevated layers during the three flights and during the observation of the smoke plume from Central America at GIF are listed in Table 2. The average aerosol number size distributions are shown in Figure 10.

[20] The aerosol scattering coefficients observed in the plumes generated by fire activities ranged from 235 to nearly 500 Mm^{-1} . For the elevated plumes from East Asia, the aerosol size distributions showed large accumulation-mode diameters, near 400 nm. In contrast, the aerosol

Table 2. Aerosol Optical Properties Averaged Over Elevated Layers During Three Flights and During the Observation of Plumes From Central America at the GIF

Date	Altitude, m	$\sigma_{\text{sp}}^{\text{a}}$, Mm^{-1}	$\sigma_{\text{ap}}^{\text{a}}$, Mm^{-1}	Single Scattering Albedo	$f(\text{RH})$ (85%/40%)
25 May 2003	3568	497.2 ^b	21.1 ^b	0.96 ^b	1.20 ^c
27 May 2003	3041	235.0 ^b	9.2 ^b	0.96 ^b	1.15 ^c
28 May 2003	4132	292.7 ^b	9.4 ^b	0.97 ^b	1.20 ^c
9 May 2003	ground (SGP)	359.8 ^d	21.9 ^d	0.94 ^d	1.30 ^d

^aAt STP (0°C and 1 atm = 101,325 Pa).

^bAt 530 nm.

^cAt 540 nm.

^dAt 550 nm.

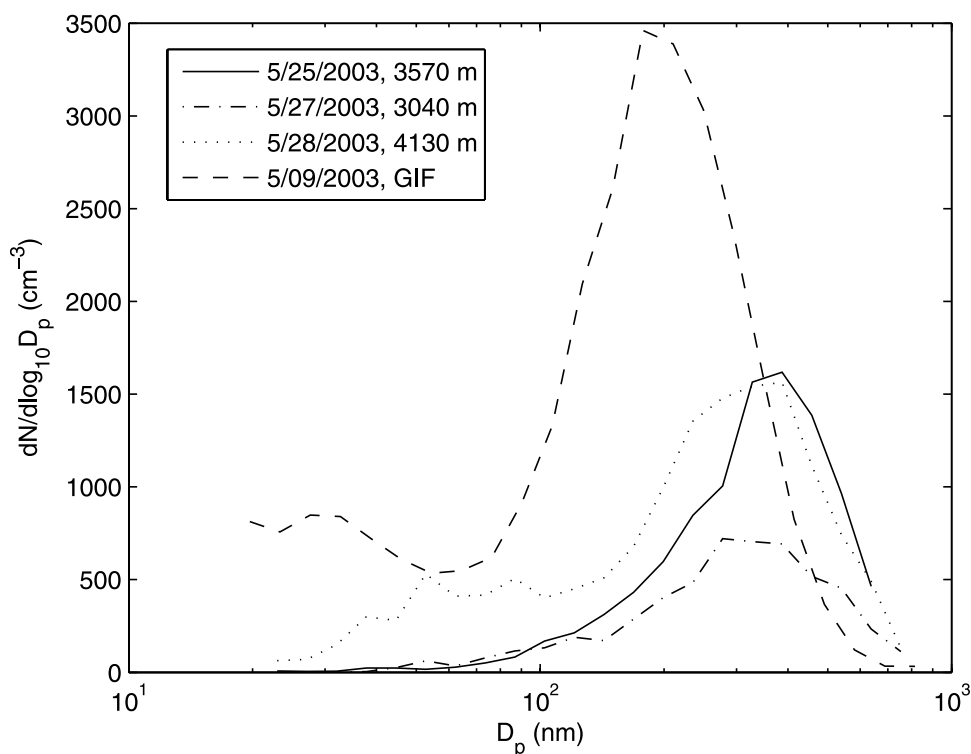


Figure 10. Aerosol number size distributions averaged over elevated layers during three flights and during the observation of plumes from Central America at the GIF.

observed in plumes originating from wildfire at Central America exhibited a substantially smaller accumulation-mode diameter, around 200 nm. The difference in particle sizes observed within the Central American and Asian plumes is possibly due to different fire types and strengths. The difference in the initial scavenging in pyrocumulus clouds and the scavenging during the long-range transport could also lead to the observed differences in aerosol size distributions. As expected, the aerosols within the elevated plumes had similar intensive properties: the aerosol single scattering albedo ranged from 0.96 to 0.97 and the scattering $f(\text{RH})$ ranged from 1.15 to 1.20. The scattering $f(\text{RH})$ is defined as the ratio of aerosol scattering coefficient at 85% RH to that at 40% RH. The aerosol single scattering albedo derived from in situ measurements of aerosol scattering and absorption agree with values retrieved from Lidar measurement at the SGP for the elevated layers [Ferrare *et al.*, 2006b]. The high aerosol single scattering albedo indicates the aerosol within the layers were relatively nonabsorbing. Similar values of single scattering albedo for this smoke were also found using multiwavelength lidar retrievals for lidar data acquired over Tokyo, Japan and Leipzig, Germany [Murayama *et al.*, 2004; Mattis *et al.*, 2003]. For plumes from Central America, the aerosol single scattering albedo showed a similar value of 0.94, and the scattering $f(\text{RH})$ measured by AOS was 1.30.

3.5. Study of Aerosol Evolution Through Growth Law Analysis

[21] When the primary aerosol emission and coagulation are negligible, and the growth of the aerosol particles is

controlled mainly by gas-to-particle conversion, the particle growth rate can be determined from the time series of the aerosol size distribution [McMurry *et al.*, 1981; Wilson and McMurry, 1981; McMurry and Wilson, 1982]. This technique, which is often referred to as growth law analysis, has been previously applied to observations of particle growth in power plant plumes, and in ground based and aircraft based studies [McMurry *et al.*, 1981; Wilson and McMurry, 1981; McMurry and Wilson, 1982; Brock *et al.*, 2002]. The goal of the analysis is to determine the relationship between the growth rate of particle diameter and the diameter of the particle. By comparing this relationship to different gas-to-particle conversion mechanisms, it is possible to determine the mechanism responsible for the observed growth [McMurry *et al.*, 1981; Wilson and McMurry, 1981; McMurry and Wilson, 1982; Brock *et al.*, 2002]. The particle diameter growth rate is determined from the rate of the size distribution change as [McMurry and Wilson, 1982]:

$$\frac{dD_p}{dt} = \frac{N_g(D_p, t_2) - N_g(D_p, t_1)}{(t_2 - t_1)n_{av}(D_p)} \quad (3)$$

where D_p is the particle diameter, N_g the number of particle per cm^3 of air with diameter greater than D_p , and t_2 and t_1 are the times when measurements were made. $n_{av}(D_p)$ is the average size distribution from t_1 to t_2 :

$$n_{av}(D_p) = \frac{1}{t_2 - t_1} \int_{t_1}^{t_2} -\frac{\partial N_g(D_p, t)}{\partial D_p} dt \quad (4)$$

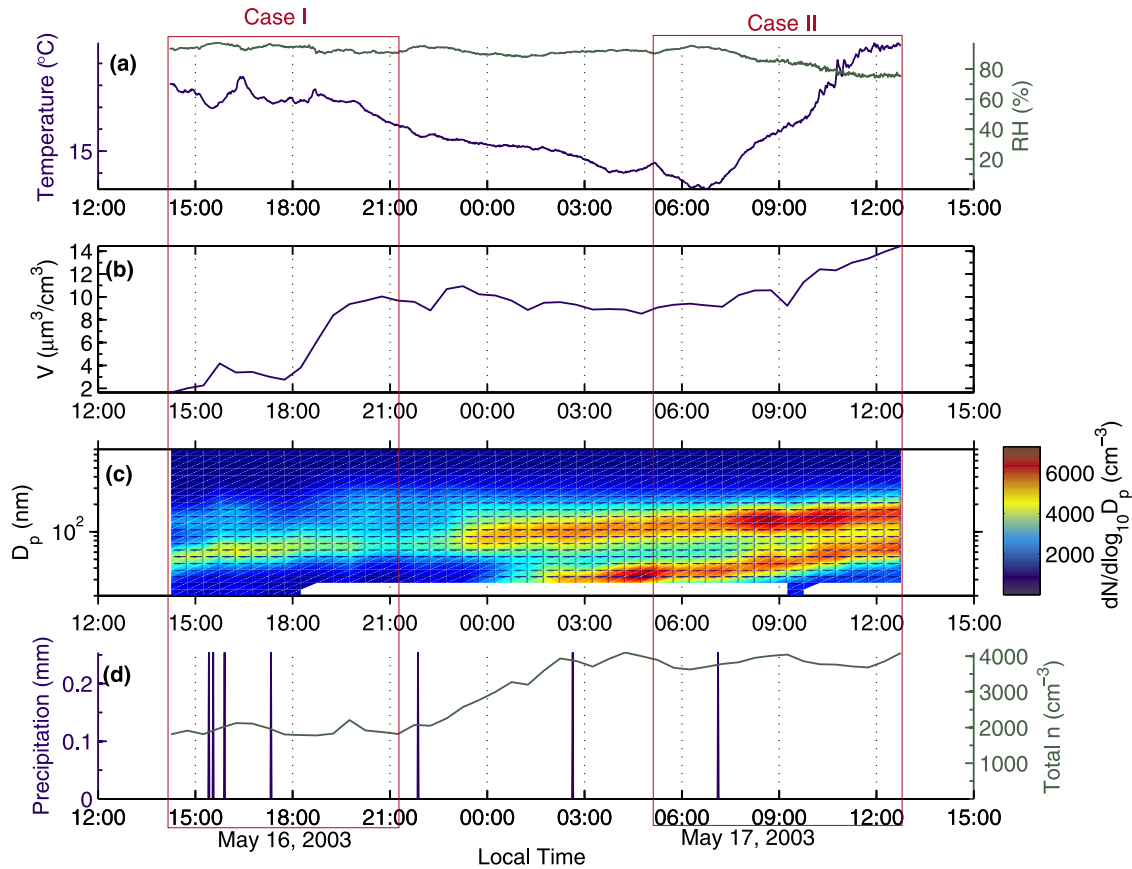


Figure 11. Measurements from 16 May at 1200 LT to 17 May at 1500 LT. (a) Ambient temperature and RH. (b) Submicrometer aerosol volume concentrations calculated from aerosol number size distributions. (c) Aerosol number size distributions, with the color indicating the number concentration. (d) Total particle number concentration ($D_p > 10$ nm) and precipitation.

A discussion of the diameter growth rates under different mechanisms is given by *McMurry and Wilson* [1982]. For condensation controlled growth, the particle diameter growth rate is described by following semiempirical relation [*Bademosi and Liu*, 1971]:

$$\frac{dD_p}{dt} \propto \frac{1}{D_p} \left(\frac{1.51 + 2.08Kn}{1.51 + Kn(1.08 + 6.04\beta) + 8.32\beta Kn^2} \right) \quad (5)$$

where $K_n = 2\lambda/D_p$, and $\beta = \frac{D}{c\lambda}$, λ is the mean free path, D the diffusivity, and c the mean thermal velocity of the condensing species. For condensation controlled growth, the diameter growth rate is independent of particle size in the free molecular regime ($D_p \ll \lambda$), and decreases proportional to $1/D_p$ in the continuum regime ($D_p \gg \lambda$). As the SGP site was in the vicinity of several power plants, and high SO_2 mixing ratio was frequently observed during the IOP, one of the likely condensing species is the H_2SO_4 formed through the gas phase oxidation of SO_2 . The diffusivity of hydrated sulfuric acid vapor in air has been experimentally determined to be $0.077 \text{ cm}^2 \text{ s}^{-1}$ [*Hanson and Eisele*, 2000].

[22] If the particle growth is due to volume controlled reaction/growth (i.e., aqueous reaction within hydrated

particles, gas/particle partitioning), the corresponding growth rate is expressed as [*McMurry and Wilson*, 1982]:

$$\frac{dD_p}{dt} \propto D_p \quad (6)$$

[23] Using the continuous aerosol size distribution measured at the GIF, growth law analyses were performed in periods during which the assumptions for growth analysis were satisfied. The assumptions are (1) during the chosen periods, the primary particle emissions and coagulation were not significant, as evidenced by size distributions and a constant total particle number concentration; (2) the growth of the particles over the measurement period was substantial, such that the growth rates derived are statistically significant; and (3) there is no significant dilution or change of air mass, as evidenced by a constant total particle number concentration. On the basis of these criteria, four cases are chosen for growth law analysis; the results are presented below.

3.5.1. Case I of Growth Law Analysis, 16 May 2003

[24] The first case analyzed is from 1415 to 2115 LT on 16 May. During the period, the sky was overcast with occasional light drizzle, and the aerosol size distribution showed continuous particle growth (Figure 11). The cloud

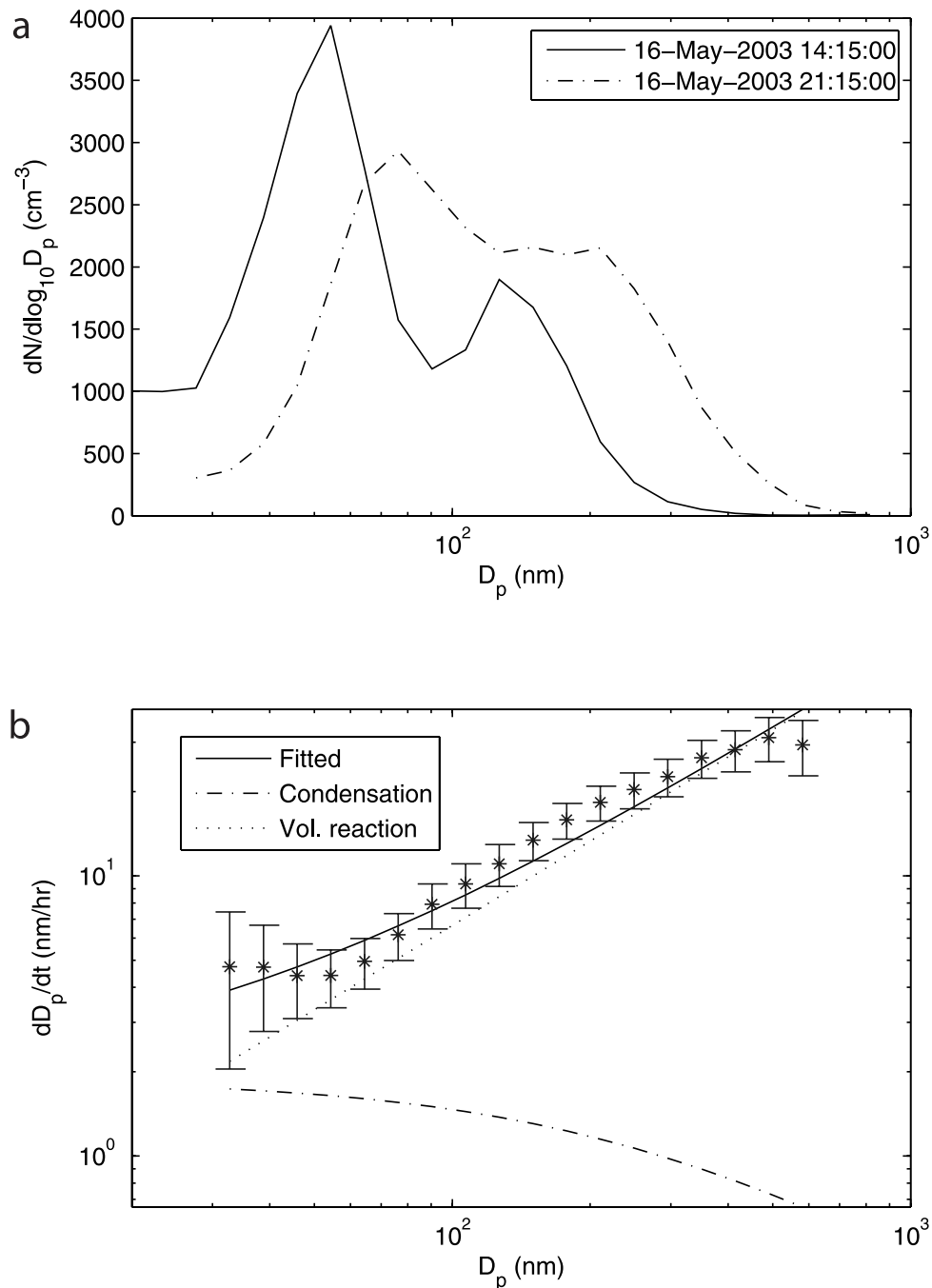


Figure 12. (a) Aerosol size distributions at the beginning and the end of the first case for growth law analysis and (b) derived particle growth rate and the least squares fit to growth rates of condensational processes (equation (5)) and volume-based reactions (equation (6)).

was dominated by midlevel convective precipitating systems with some low-level stratus. The cloud coverage was 100%, and the base height of the stratus cloud was around 300 m (AGL). On the basis of the measured precipitation rate, the calculated scavenging coefficient is less than 9×10^{-3} /hr for particles ranging from 20 nm to $1 \mu\text{m}$ in diameter, and the effect of scavenging from the drizzle is negligible on particle size distribution during this period. The aerosol total number concentration, which was measured by a condensation particle counter (CPC), remained constant at around 2000 cm^{-3} ,

suggesting primary particle emission, coagulation, and wet scavenging are negligible. Figure 12 presents the particle size distributions at the beginning and the end of the period; size distributions were bimodal throughout the period. Substantial growth was observed for both modes. The mode diameter of the Aitken mode grew from 54 to 76 nm and the mode diameter of the accumulation mode increased from 127 to 208 nm. Figure 12 also shows the particle growth rates derived using equation (3). The uncertainties in derived growth rate are estimated on the basis of counting statistics

and sizing accuracy of the SMPS system, and the variation of particle concentration derived from the total particle concentrations. A least squares fit of the diameter growth rate shows the size dependence of the growth rate is well represented by a combination of condensation growth and volume controlled reaction:

$$\begin{aligned} \frac{dD_p}{dt} &= \left. \frac{dD_p}{dt} \right|_C + \left. \frac{dD_p}{dt} \right|_{V.R.} \\ \left. \frac{dD_p}{dt} \right|_C &= a \cdot \frac{1}{D_p} \left(\frac{1.51 + 2.08Kn}{1.51 + Kn(1.08 + 6.04\beta) + 8.32\beta Kn^2} \right) \quad (7) \\ \left. \frac{dD_p}{dt} \right|_{V.R.} &= b \cdot D_p \end{aligned}$$

where $\left. \frac{dD_p}{dt} \right|_C$ and $\left. \frac{dD_p}{dt} \right|_{V.R.}$ are the fitted particle diameter growth rates due to condensation and volume controlled reactions, respectively, and a and b are fitted coefficients. The fractional contribution of the volume controlled reaction to the increase of the aerosol volume concentration is given by:

$$f_{V.R.} = \frac{\int_{D_{p1}}^{D_{p2}} D_p^2 \left. \frac{dD_p}{dt} \right|_{V.R.} n_{av}(D_p, t) dD_p}{\int_{D_{p1}}^{D_{p2}} D_p^2 \left[\left. \frac{dD_p}{dt} \right|_{V.R.} + \left. \frac{dD_p}{dt} \right|_C \right] n_{av}(D_p, t) dD_p} \quad (8)$$

where $n_{av}(D_p, t)$ is the average particle size distribution during the period. For this case, the $f_{V.R.}$ is 94%, suggesting the increase of aerosol volume concentration was dominated by volume controlled reactions.

[25] Size resolved aerosol chemical composition was inferred from aerosol hygroscopicity measured by a Tandem Differential Mobility Analyzer system at the GIF during the IOP [Gasparini *et al.*, 2004, 2006]. In their analysis, Gasparini *et al.* assumed that the particles consisted of ammonium sulfate and a group of low-hygroscopic species, which showed hygroscopic growth factors (ratio of particle diameter at 85% RH to that at 40%) less than 1.1 [Gasparini *et al.*, 2004]. As the hygroscopic growth of ammonium sulfate is well known, size resolved sulfate volume fraction can be derived from the measured aerosol hygroscopicity [Gasparini *et al.*, 2004]. The assumption of sulfate being the only inorganic hygroscopic species is supported by the following: (1) The contribution of sea salt to the aerosol mass is negligible given the inland location of the SGP site, (2) the chemical composition of submicrometer aerosol measured by a Particle Into Liquid Sampler (PILS) at the GIF showed the contributions of both sea salt and nitrate were small, and (3) the sulfate was often completely neutralized by ammonium. On the basis of the sulfate fraction derived from aerosol hygroscopicity, at the beginning of the first case, 1415 LT on 16 May, the volume concentration of sulfate and low-hygroscopic species are calculated as 1.01 and 0.64 $\mu\text{m}^3/\text{cm}^3$, respectively. The volume concentrations of sulfate and low-hygroscopic species increased to 6.76 and 2.92 $\mu\text{m}^3/\text{cm}^3$ at 2115 LT. Sulfate represents 72% of the total increase in aerosol volume concentration.

[26] The dominance of sulfate in the increase of aerosol volume concentration, together with the volume controlled reaction mechanism inferred from growth law analysis,

suggests aqueous oxidations of SO_2 by H_2O_2 and/or O_3 within hydrated aerosol particles a possible source of the observed sulfate. The conclusion is also supported by the high RH observed during this period, which is averaged at 94% at surface. As a result of adiabatic cooling, the ambient RH increased with increasing altitude, and reached 100% at the cloud base, indicating enhanced SO_2 oxidation rate due to higher liquid water content in hydrated particles. The nearly 100% cloud coverage and the bimodal size distributions observed during the period also suggest possible in cloud production of sulfate through aqueous oxidation of SO_2 . As suggested by Hoppel *et al.* [1986], the larger cloud condensation nuclei (CCN) grew through aqueous phase reactions in clouds to form the larger accumulation mode, while the small non-CCN grew at slower pace through condensation process, and became the Aitken mode. Measurements on board the BBSS at 1230 and 1830 LT showed uniform potential temperature and water vapor mixing ratio within the boundary layer, indicating a well mixed boundary layer. After particles grew through aqueous reaction in high RH region and in clouds, they were transported down to the surface through detrainment and mixing process, which explains the observed particle growth at the GIF. For in cloud production of sulfate dominated by the aqueous reaction of SO_2 and H_2O_2 , the particle volume growth rate is proportional to the product of the cloud droplet volume and the fraction of time during which particles are activated into cloud droplets:

$$\frac{dV}{dt} = \frac{\pi}{2} D_p^2 \frac{dD_p}{dt} \propto \frac{\pi}{6} D_d^3 \cdot f_i \quad (9)$$

where D_d is the droplet diameter after particles are activated and f_i is the fraction of time when particles are activated. The particle diameter growth rate is derived as:

$$\frac{dD_p}{dt} \propto \frac{D_d^3}{D_p^2} f_i \quad (10)$$

On the basis of condensation of supersaturated water vapor, adiabatic cloud models often predict narrow droplet size distributions in clouds (i.e., CCN of different diameters are activated and form cloud droplets with similar diameters). However, many field studies have shown cloud droplet size distributions observed had higher dispersions than those predicted by the models [Martin *et al.*, 1994; Hudson and Svensson, 1995; Politovich 1993; Hudson and Yum, 1997]. Larger CCN are likely activated and form larger cloud droplets. Moreover, as aerosol particles experience different water vapor supersaturations due to inhomogeneity of updraft velocity and turbulence, larger particles were more likely to be activated into cloud droplets and the fraction of time (f_i) during which they remain as cloud droplets is higher than that of smaller particles. Both larger droplet size and higher f_i lead to higher aqueous sulfate production rate, and possibly result in increased particle diameter growth rate as increasing diameter, as shown by growth law analysis. Similar particle growth law showing combination of condensational growth and volume controlled reactions have been observed in previous field studies [McMurry *et al.*, 1981; McMurry and Wilson, 1982] including a study of

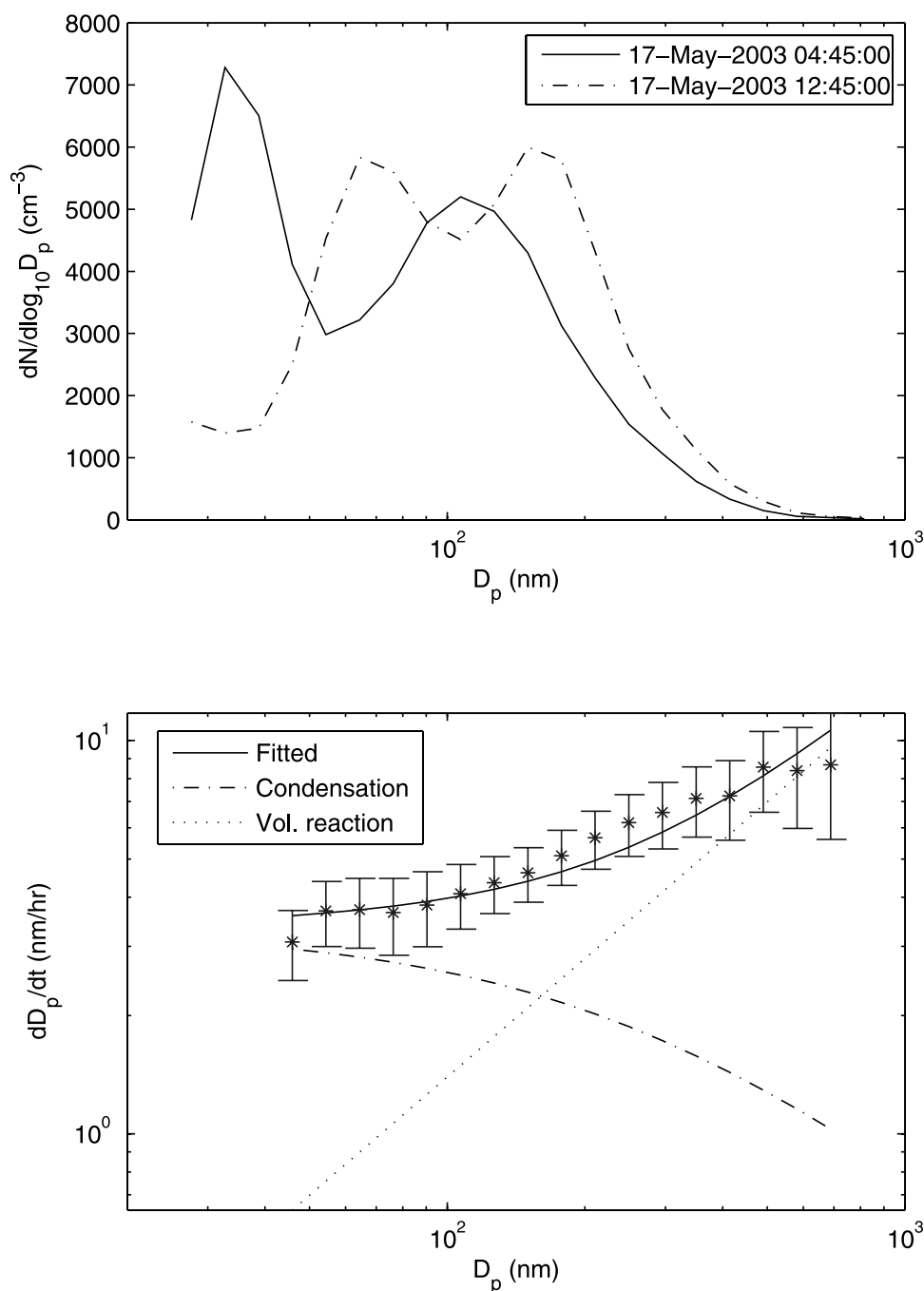


Figure 13. Same as Figure 12 for the measurements from 0445 to 1245 LT on 17 May (the second case).

aerosol growth during a winter fog event [Ulevicius *et al.*, 1994].

[27] Besides sulfate, the volume concentration of low-hygroscopic species also increased substantially from 0.64 to $2.92 \mu\text{m}^3/\text{cm}^3$. As the contributions from mineral dust and elemental carbon to submicrometer aerosol volume concentration are small at the SGP, we think most of the low-hygroscopic species were organics, which were likely formed through partitioning of secondary organics into the particle phase. As the volume growth resulting from the partitioning of secondary organics increases with the in-

creasing volume of preexisting organic species within the particle [Pankow, 1994], the rate of particle growth due to gas/particle partitioning has the same size dependence (growth law) as those under volume controlled reactions. Size resolved chemical speciation, which were not available during the IOP, would be able to provide more information regarding the mechanisms responsible for the increase of low-hygroscopic volume concentration.

3.5.2. Case II of Growth Law Analysis, 17 May

[28] The second case analyzed is from 0445 to 1245 LT on 17 May. The sky was overcast with stratus cloud base

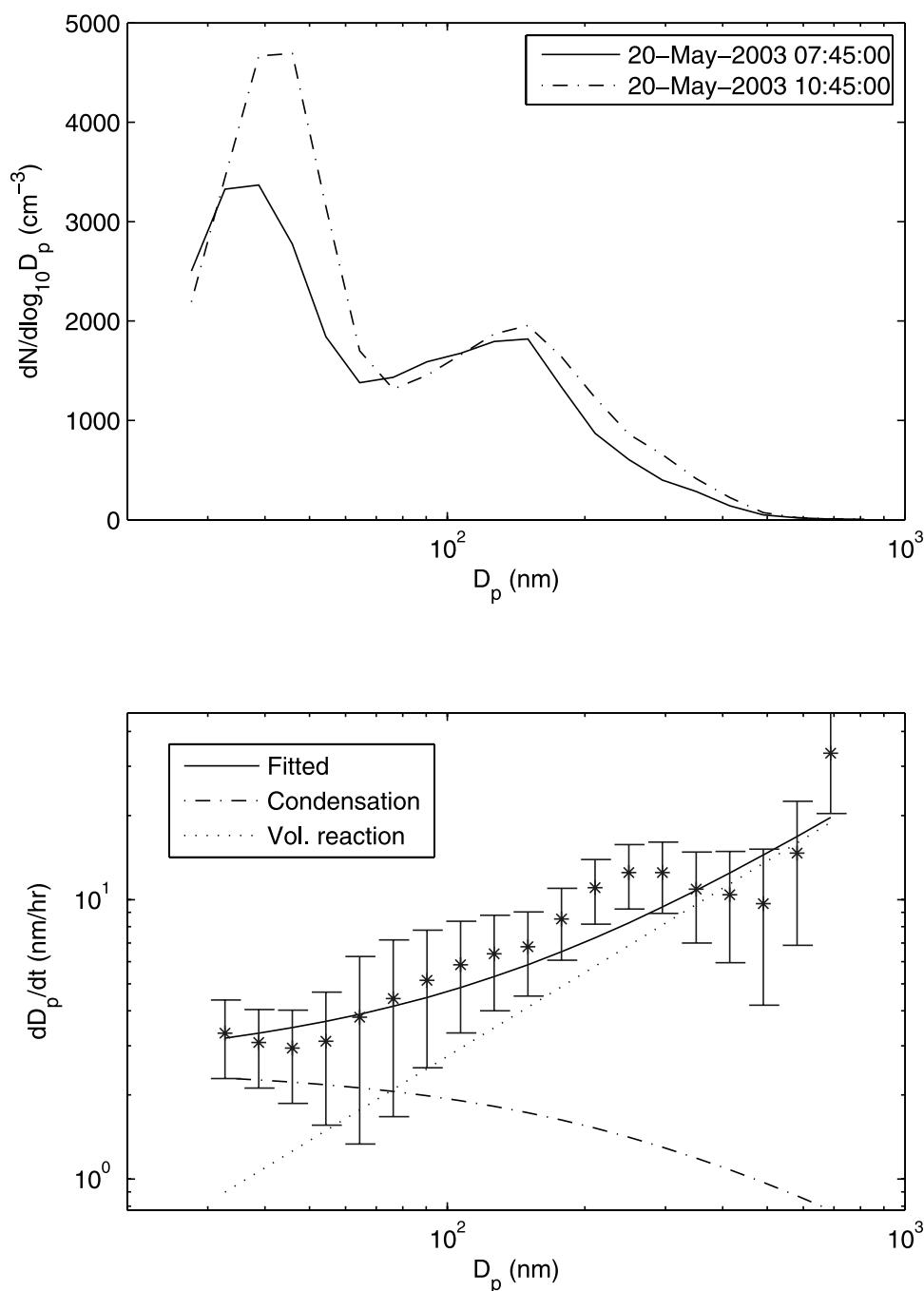


Figure 14. Same as Figure 12 for the measurements from 0745 to 1045 on 20 May (the third case).

height at around 500 m (AGL). The average RH reached 86% at the surface during this period. The aerosol size distribution, submicrometer volume concentration, and total number concentration are presented in Figure 11. Similar to the first case, aerosol size distributions were bimodal. Figure 13 shows size distributions at the beginning and the end of the period, along with the derived diameter growth rate. The particle growth rate is again well represented by a combination of condensation growth and volume controlled reactions. While the volume controlled reactions and/or gas/particle partitioning still dominated the overall particle growth, their contributions to the total increases in

aerosol volume concentration decreased from 94% in the first case to 64%. On the basis of aerosol hygroscopicity measurements, the sulfate volume concentration increased $4.2 \mu\text{m}^3/\text{cm}^3$ from $5.6 \mu\text{m}^3/\text{cm}^3$ to $9.8 \mu\text{m}^3/\text{cm}^3$, which represents 71% of the total increase in volume concentration. Given the high RH and nearly 100% cloud coverage, and the dominance of sulfate in the increased aerosol volume concentration, the sulfate, at least partially, was produced through aqueous oxidation of SO_2 . Without further information, we cannot determine the species that were involved in the condensational growth. One of the

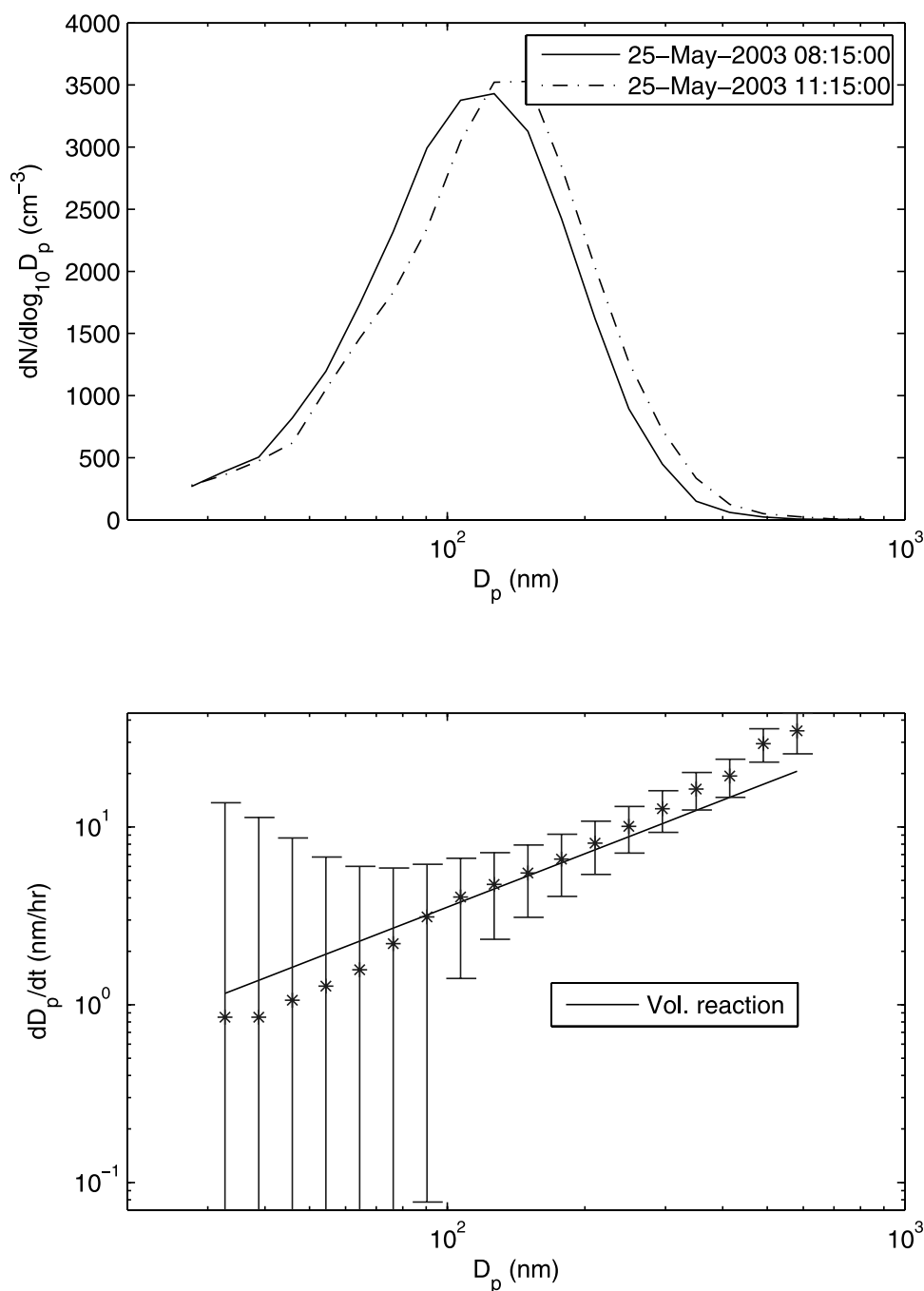


Figure 15. Same as Figure 12 for the measurements from 0815 to 1115 on 25 May (the fourth case).

possible condensing species is H_2SO_4 , produced through gas phase reaction of SO_2 and OH.

[29] No significant particle growth was observed and the submicrometer aerosol volume concentration remained nearly constant before 0715 LT. Vertical profiles of potential temperature and water vapor mixing ratio showed a stable boundary layer at 0630 LT. The boundary layer became well mixed at 1255 LT, which is evidenced by the uniform potential temperature and water vapor mixing ratio within the boundary layer. The constant submicrometer aerosol volume concentration observed could be explained by the following. First, aqueous production of sulfate is expected

to be most significant within the clouds and in the regions below clouds where RH is nearly 100%, and a stable boundary layer prevented aerosol processed by the clouds and within high RH regions, if any, to reach the surface level; second, aqueous production of sulfate was most likely dominated by the reaction of SO_2 and H_2O_2 . As the H_2O_2 is produced in sunlight, we do not expect substantial aqueous production of sulfate in the early morning. After 0715 LT, the boundary layer gradually became well mixed because of the solar heating of the surface. The aerosol particles processed in clouds and regions with high RH were then

Table 3. Summary of Particle Growth Law Analysis Using Size Distributions Measured at the GIF During the IOP

Date	Period, LT	Air Mass	Growth Mechanisms	$f_{V.R.}$, %	ΔV , $\mu\text{m}^3/\text{cm}^3$	$\Delta V(\text{sulfate})/\Delta V$, %	Cloud Coverage, %
16 May 2003 (case I)	1415–2115	midwest	condensation and volume reaction	94	8.03	72	100
17 May 2003 (case II)	0445–1245	midwest	condensation and volume reaction	64	5.91	71	100
20 May 2003 (case III)	0745–1045	northwest	condensation and volume reaction	81	1.29	50	90–100
25 May 2003 (case IV)	0815–1115	midwest	volume reaction	100	1.56	57	90–100

transported down to the surface, which explains the observed particle growth at the GIF.

3.5.3. Case III and Case IV

[30] Two additional cases were analyzed for particle diameter growth rates. Both cases were in the morning with cloud coverage over 90%. Case III is from 0745 to 1045 LT on 20 May, and case IV is from 0815 to 1115 LT on 25 May. The size distributions and calculated diameter growth rates are given in Figures 14 and 15. Because of the shorter growth time, the particle growth observed during cases III and IV is substantially less than that during cases I and II. As a result, the uncertainties in derived diameter growth rates are significantly higher. Least squares fits of the diameter growth rates indicate the particle growth in case III was due to a combination of condensation and volume controlled reactions, whereas the particle growth in case IV is a result of volume controlled reactions only. For case IV, the uncertainty in derived diameter growth rate increases significantly with decreasing particle diameter, especially for diameters less than 100 nm. As the diameter growth rate is the highest at the small particle size range under condensation processes, we cannot exclude the possibility of condensational growth because of the large uncertainties in diameter growth rates at small particle sizes. However, for both cases, the uncertainties in diameter growth rates are small for particles larger than 100 nm, and the volume controlled reactions dominate the particle growth, especially for particles having diameters larger than 100 nm.

[31] The results of growth law analyses are summarized in Table 3. For all four cases analyzed, the volume controlled reactions dominate the overall increases in aerosol volume concentration. On the basis of chemical composition inferred from hygroscopicity measurements, ammonium sulfate contributes to 50–72% of the total aerosol volume concentration increase. Extensive cloud coverage and high RH below the clouds suggest the sulfate was likely produced through aqueous oxidation of SO_2 in cloud droplets and hydrated aerosol particles. The produced sulfate was then transported down to the surface as a result of mixing process within the boundary layer. Besides sulfate, low-hygroscopic species also contributed significantly to the increases of aerosol volume concentration (28–50%). On the basis of the particle growth law, the increases in volume concentration of low-hygroscopic species were likely due to the partitioning of the secondary organic species into the particle phase. For all four cases analyzed, the condensational growth had small contributions to the overall particle growth. Given the high cloud coverage during the periods analyzed, it is expected that the growth due to condensation was less important as the actinic flux and photochemical reaction rates were low. For comparison, it would be interesting to study the particle growth rates when cloud coverage was low. Unfortunately, no such case satisfying

the assumptions for growth law analysis was available during the IOP. Future work will include studies of particle growth rates and mechanisms under different meteorological conditions and at various locations.

4. Conclusions

[32] Aerosol size distributions were measured continuously at the GIF and on board the Twin Otter aircraft at the SGP site during May 2003, as part of the Aerosol Intensive operation period of the DOE ARM program. Large variations in aerosol properties, including size distribution and optical properties were observed. Using simultaneous trace gas measurements and back trajectory analyses, the aerosol properties were found to be influenced by both local and long-range sources. The aerosol from the southeast was found to be influenced by wild fires in Central America. Aerosol with high scattering coefficients (up to 500 Mm^{-1}), which can be traced back to forest fires in East Asia, was also observed at altitudes above 3000 m. These aerosols had large mode diameters near 400 nm in diameter, and were most likely aged in plumes during their long transport over the Pacific Ocean from East Asia. High particle concentrations observed during the IOP were well correlated with high SO_2 mixing ratios, suggesting nucleation involving sulfuric acid is likely the main source of newly formed particles. The high SO_2 concentrations were observed when the wind was from the east, south, and southeast, where several power plants are located.

[33] Detailed growth law analyses were carried out for four periods, during which nearly 100% cloud coverage was observed. The results indicate the particle growth in the four cases was due to a combination of condensation and volume controlled reactions, and the volume controlled reactions dominated the overall growth. Besides sulfate, low-hygroscopic species, likely secondary organics, also contributed substantially to the particle growth. For two cases, the low-hygroscopic species accounted for nearly 50% percent of the total increases in aerosol volume concentration. The growth laws and meteorological conditions indicate the sulfate was mainly produced through aqueous oxidation of SO_2 in cloud droplets and hydrated aerosol particles, and the increases in low-hygroscopic volume concentration were likely due to partitioning of secondary organic species into the particles. The results from growth law analyses suggest when the cloud coverage is high, the fractional contribution of condensational growth to overall particle growth are small at the SGP.

[34] **Acknowledgments.** This paper has been authored with support from the Office of Biological and Environmental Research under contract DE-AC02-98CH10866 and DE-AC06-76RL01830 (ITF#5788) with the U.S. Department of Energy. We thank Steve Schwartz, Larry Kleinman, Yin-Nan Lee, and Peter Daum for their comments on this manuscript and

Mike Jensen for providing meteorological information during the IOP. The authors also acknowledge the U.S. Department of Energy ARM program for providing support at the SGP site and for aircraft measurements.

References

- Andrews, E., P. J. Sheridan, J. A. Ogren, and R. Ferrare (2004), In situ aerosol profiles over the Southern Great Plains cloud and radiation test bed site: 1. Aerosol optical properties, *J. Geophys. Res.*, *109*, D06208, doi:10.1029/2003JD004025.
- Andrews, E., et al. (2006), Comparison of methods for deriving aerosol asymmetry parameter, *J. Geophys. Res.*, *111*, D05S04, doi:10.1029/2004JD005734.
- Bademosi, F., and B. Y. H. Liu (1971), Diffusion charging of Knudsen aerosols - I. (Experiment) and II. (Theory), *Publ. 155*, 156 pp., Particle Technol. Lab., Minneapolis, Minn.
- Bench, G., P. G. Grant, D. Ueda, S. S. Cliff, K. D. Perry, and T. A. Cahill (2001), The use of STIM and PESA to respectively measure profiles of aerosol mass and hydrogen content across Mylar rotating drum impactor samples, *Aerosol Sci. Technol.*, *36*, 642–651.
- Bergin, M. H., S. E. Schwartz, R. N. Halthore, J. A. Ogren, and D. L. Hlavka (2000), Comparison of aerosol optical depth inferred from surface measurements with that determined by Sun photometry for cloud-free conditions at a continental U.S. site, *J. Geophys. Res.*, *105*(D5), 6807–6816.
- Bluth, R. T., P. A. Durkee, J. H. Seinfeld, R. C. Flagan, L. M. Russell, P. A. Crowley, and P. Finn (1996), Center for Interdisciplinary Remotely-Piloted Aircraft Studies (CIRPAS), *Bull. Am. Meteorol. Soc.*, *77*(11), 2691–2699.
- Brock, C. A., et al. (2002), Particle growth in the plumes of coal-fired power plants, *J. Geophys. Res.*, *107*(D12), 4155, doi:10.1029/2001JD001062.
- Cahill, T. A., and P. Wakabayashi (1993), Compositional analysis of size-segregated aerosol samples, in *Measurement Challenges in Atmospheric Chemistry*, edited by L. Newman, pp. 211–228, John Wiley, Hoboken, N. J.
- Cahill, T. A., C. Goodart, J. W. Nelson, R. A. Eldred, J. S. Nasstrom, and P. J. Feeney (1985), Design and evaluation of the drum impactor, *Proceedings of International Symposium on Particulate and Multi-phase Processes*, vol. 2, edited by T. Ariman and T. Nejat Veziroglu, pp. 319–325, Taylor and Francis, Philadelphia, Pa.
- Clarke, A. D., V. N. Kapustin, F. L. Eisele, R. J. Weber, and P. H. McMurry (1999), Particle production near marine clouds: Sulfuric acid and predictions from classical binary nucleation, *Geophys. Res. Lett.*, *26*(16), 2425–2428.
- Collins, D. R., R. C. Flagan, and J. H. Seinfeld (2002), Improved inversion of scanning DMA data, *Aerosol Sci. Technol.*, *36*(1), 1–9.
- Damoah, R., et al. (2004), Around the world in 17 days - Hemispheric-scale transport of forest fire smoke from Russia in May 2003, *Atmos. Chem. Phys.*, *4*, 1311–1321.
- Dorling, S. R., T. D. Davies, and C. E. Pierce (1992), Cluster-analysis - A technique for estimating the synoptic meteorological controls on air and precipitation chemistry - Method and applications, *Atmos. Environ., Part A*, *26*(14), 2575–2581.
- Draxler, R. R. (1988), Hybrid Single-Parcel Lagrangian Integrated Trajectories (HYSPLIT): Model description, technical memorandum, Natl. Oceanic and Atmos. Admin., Washington, D. C.
- Feingold, G., W. L. Eberhard, D. E. Veron, and M. Previdi (2003), First measurements of the Twomey indirect effect using ground-based remote sensors, *Geophys. Res. Lett.*, *30*(6), 1287, doi:10.1029/2002GL016633.
- Ferrare, R. A., G. Feingold, S. Ghan, J. A. Ogren, S. E. Schwartz, B. Schmid, and P. Sheridan (2006a), Preface to special section: Atmospheric Radiation Measurement Program May 2003 Intensive Operations Period examining aerosol properties and radiative influences, *J. Geophys. Res.*, *111*, D05S01, doi:10.1029/2005JD006908.
- Ferrare, R. A., et al. (2006b), Evaluation of daytime measurements of aerosols and water vapor made by an operational Raman lidar over the southern Great Plains, *J. Geophys. Res.*, *111*, D05S08, doi:10.1029/2005JD005836.
- Gasparini, R., R. J. Li, and D. R. Collins (2004), Integration of size distributions and size-resolved hygroscopicity measured during the Houston Supersite for compositional categorization of the aerosol, *Atmos. Environ.*, *38*(20), 3285–3303.
- Gasparini, R., R. J. Li, D. R. Collins, and R. A. Ferrare (2006), Aerosol hygroscopicity and volatility measured at the ARM SGP site and their application to investigate composition and evolution, *J. Geophys. Res.*, *111*, D05S12, doi:10.1029/2004JD005448.
- Hanson, D. R., and F. Eisele (2000), Diffusion of H₂SO₄ in humidified nitrogen: Hydrated H₂SO₄, *J. Phys. Chem. A*, *104*(8), 1715–1719.
- Hegg, D. A., D. S. Covert, H. Jonsson, and P. A. Covert (2005), Determination of the transmission efficiency of an aircraft aerosol inlet, *Aerosol Sci. Technol.*, *39*(10), 966–971.
- Hinds, W. C. (1999), *Aerosol Technology*, pp. 260–265, 285–288 John Wiley, Hoboken, N. J.
- Hoppel, W. A., G. M. Frick, and R. E. Larson (1986), Effect of nonprecipitating clouds on the aerosol size distribution in the marine boundary-layer, *Geophys. Res. Lett.*, *13*(2), 125–128.
- Hudson, J. G., and G. Svensson (1995), Cloud microphysical relationships in California marine stratus, *J. Appl. Meteorol.*, *34*(12), 2655–2666.
- Hudson, J. G., and S. S. Yum (1997), Droplet spectral broadening in marine stratus, *J. Atmos. Sci.*, *54*(22), 2642–2654.
- Intergovernmental Panel on Climate Change (2001), *Climate Change 2001: The Scientific Basis*, Cambridge Univ. Press, New York.
- Jaffe, D., I. Bertsch, L. Jaeglé, P. Novelli, J. S. Reid, H. Tanimoto, R. Vingarzan, and D. L. Westphal (2004), Long-range transport of Siberian biomass burning emissions and impact on surface ozone in western North America, *Geophys. Res. Lett.*, *31*, L16106, doi:10.1029/2004GL020093.
- Kim, B. G., S. E. Schwartz, M. A. Miller, and Q. L. Min (2003), Effective radius of cloud droplets by ground-based remote sensing: Relationship to aerosol, *J. Geophys. Res.*, *108*(D23), 4740, doi:10.1029/2003JD003721.
- Kulmala, M., P. Korhonen, I. Napari, A. Karlsson, H. Berresheim, and C. D. O'Dowd (2002), Aerosol formation during PARFORCE: Ternary nucleation of H₂SO₄, NH₃, and H₂O, *J. Geophys. Res.*, *107*(D19), 8111, doi:10.1029/2001JD000900.
- Martin, G. M., D. W. Johnson, and A. Spice (1994), The measurement and parameterization of effective radius of droplets in warm stratocumulus clouds, *J. Atmos. Sci.*, *51*(13), 1823–1842.
- Mattis, I., A. Ansmann, U. Wandinger, and D. Müller (2003), Unexpectedly high aerosol load in the free troposphere over central Europe in spring/summer 2003, *Geophys. Res. Lett.*, *30*(22), 2178, doi:10.1029/2003GL018442.
- McMurry, P. H., and J. C. Wilson (1982), Growth laws for the formation of secondary ambient aerosols—Implications for chemical conversion mechanisms, *Atmos. Environ.*, *16*, 121–134.
- McMurry, P. H., D. J. Rader, and J. L. Stith (1981), Studies of aerosol formation in power-plant plumes. I. Growth laws for secondary aerosols in power-plant plumes—Implications for chemical conversion mechanisms, *Atmos. Environ.*, *15*, 2315–2327.
- Murayama, T., D. Müller, K. Wada, A. Shimizu, M. Sekiguchi, and T. Tsukamoto (2004), Characterization of Asian dust and Siberian smoke with multi-wavelength Raman lidar over Tokyo, Japan in spring 2003, *Geophys. Res. Lett.*, *31*, L23103, doi:10.1029/2004GL021105.
- Pankov, J. F. (1994), An absorption-model of the gas aerosol partitioning involved in the formation of secondary organic aerosol, *Atmos. Environ.*, *28*(2), 189–193.
- Politovich, M. K. (1993), A study of the broadening of droplet size distributions in cumuli, *J. Atmos. Sci.*, *50*(14), 2230–2244.
- Raabe, O. G., D. A. Braaten, R. L. Axelbaum, S. V. Teague, and T. A. Cahill (1988), Calibration studies of the DRUM impactor, *J. Aerosol Sci.*, *19*(2), 183–195.
- Schmid, B., et al. (2005), How well do state-of-the-art techniques measuring the vertical profile of tropospheric aerosol extinction compare?, *J. Geophys. Res.*, *111*, D05S07, doi:10.1029/2005JD005837.
- Sheridan, P. J., D. J. Delene, and J. A. Ogren (2001), Four years of continuous surface aerosol measurements from the Department of Energy's Atmospheric Radiation Measurement Program Southern Great Plains Cloud and Radiation Testbed site, *J. Geophys. Res.*, *106*(D18), 20,735–20,747.
- Turner, D. D., R. A. Ferrare, and L. A. Brasseur (2001), Average aerosol extinction and water vapor profiles over the southern Great Plains, *Geophys. Res. Lett.*, *28*(23), 4441–4444.
- Turner, D. D., R. A. Ferrare, L. A. H. Brasseur, and W. F. Feltz (2002), Automated retrievals of water vapor and aerosol profiles from an operational Raman lidar, *J. Atmos. Oceanic Technol.*, *19*(1), 37–50.
- Ulevicuis, V., S. Trakumas, and A. Girgzdys (1994), Aerosol-size distribution transformation in fog, *Atmos. Environ.*, *28*(5), 795–800.
- Wandinger, U., et al. (2002), Optical and microphysical characterization of biomass burning and industrial pollution aerosols from multiwavelength lidar and aircraft measurements, *J. Geophys. Res.*, *107*(D21), 8125, doi:10.1029/2000JD000202.
- Wang, J., R. C. Flagan, and J. H. Seinfeld (2003), A differential mobility analyzer (DMA) system for submicron aerosol measurements at ambient relative humidity, *Aerosol Sci. Technol.*, *37*(1), 46–52.
- Wang, J., S. A. Christopher, U. S. Nair, J. S. Reid, E. M. Prins, J. Szykman, and J. L. Hand (2006), Mesoscale modeling of Central American smoke transport to the United States: 1. “Top-down” assessment of emission strength and diurnal variation impacts, *J. Geophys. Res.*, *111*, D05S17, doi:10.1029/2005JD006416.
- Weber, R. J., P. H. McMurry, R. L. Mauldin, D. J. Tanner, F. L. Eisele, A. D. Clarke, and V. N. Kapustin (1999), New particle formation in the remote

- troposphere: A comparison of observations at various sites, *Geophys. Res. Lett.*, 26(3), 307–310.
- Weber, R. J., et al. (2001), Measurements of enhanced H_2SO_4 and 3–4 nm particles near a frontal cloud during the First Aerosol Characterization Experiment (ACE 1), *J. Geophys. Res.*, 106(D20), 24,107–24,117.
- Wilson, J. C., and P. H. McMurry (1981), Studies of aerosol formation in power-plant plumes. 2. Secondary aerosol formation in the Navajo generating-station plume, *Atmos. Environ.*, 15, 2329–2339.
-
- D. Collins and R. Gasparini, Department of Atmospheric Sciences, Texas A&M University, College Station, TX 77843, USA.
- D. Covert and R. Elleman, Department of Atmospheric Sciences, University of Washington, Seattle, WA 98195, USA.
- R. A. Ferrare, NASA Langley Research Center, Hampton, VA 23681, USA.
- H. Jonsson, Naval Postgraduate School, Monterey, CA 93943, USA.
- J. Ogren and P. Sheridan, Global Monitoring Division, Earth System Research Laboratory, NOAA, Boulder, CO 80305, USA.
- S.-C. Tsay, NASA Goddard Space Flight Center, Greenbelt, MD 20771, USA.
- J. Wang, Atmospheric Science Division, Brookhaven National Laboratory, Upton, NY 11973, USA. (jian@bnl.gov)